

NOTES AND CORRESPONDENCE

Dynamical Mechanisms for the South China Sea Seasonal Circulation and Thermohaline Variabilities

PETER C. CHU, NATHAN L. EDMONS, AND CHENWU FAN

Department of Oceanography, Naval Postgraduate School, Monterey, California

14 July 1998 and 8 April 1999

ABSTRACT

The seasonal ocean circulation and the seasonal thermal structure in the South China Sea (SCS) were studied numerically using the Princeton Ocean Model (POM) with 20-km horizontal resolution and 23 sigma levels conforming to a realistic bottom topography. A 16-month control run was performed using climatological monthly mean wind stresses, restoring-type surface salt and heat, and observational oceanic inflow/outflow at the open boundaries. The seasonally averaged effects of isolated forcing terms are presented and analyzed from the following experiments: 1) nonlinear dynamic effects removed, 2) wind effects removed, and 3) open boundary inflow/outflow set to zero. This procedure allowed analysis of the contribution of individual parameters to the general hydrology and specific features of the SCS: for example, coastal jets, mesoscale topographic gyres, and countercurrents. The results show that the POM model has the capability of simulating seasonal variations of the SCS circulation and thermohaline structure. The simulated SCS surface circulation is generally anticyclonic (cyclonic) during the summer (winter) monsoon period with a strong western boundary current, a mean maximum speed of 0.5 m s^{-1} (0.95 m s^{-1}), a mean volume transport of 5.5 Sv (10.6 Sv) ($\text{Sv} \equiv 10^6 \text{ m}^3 \text{ s}^{-1}$), and extending to a depth of around 200 m (500 m). During summer, the western boundary current splits and partially leaves the coast; the bifurcation point is at 14°N in May and shifts south to 10°N in July. A mesoscale eddy on the Sunda shelf (Natuna Island eddy) was also simulated. This eddy is cyclonic (anticyclonic) with maximum swirl velocity of 0.6 m s^{-1} at the peak of the winter (summer) monsoon. The simulated thermohaline structure for summer and winter are nearly horizontal from east to west except at the coastal regions. Coastal upwelling and downwelling are also simulated: localized lifting (descending) of the isotherms and isohalines during summer (winter) at the west boundary. The simulation is reasonable when compared to the observations. Sensitivity experiments were designed to investigate the driving mechanisms. Nonlinearity is shown to be important to the transport of baroclinic eddy features, but otherwise insignificant. Transport from lateral boundaries is of considerable importance to summer circulation and thermal structure, with lesser effect on winter monsoon hydrology. In general, seasonal circulation patterns and upwelling phenomena are determined and forced by the wind, while the lateral boundary forcing plays a secondary role in determining the magnitude of the circulation velocities.

1. Introduction

The South China Sea (SCS) is a semienclosed tropical sea located between the Asian landmass to the north and west, the Philippine Islands to the east, Borneo to the southeast, and Indonesia to the south (Fig. 1), with a total area of $3.5 \times 10^6 \text{ km}^2$. It includes the shallow Gulf of Thailand and connections to the East China Sea (through the Taiwan Strait), the Pacific Ocean (through the Luzon Strait), the Sulu Sea (through the Mindoro Strait), the Java Sea (through the Gaspar and Karimata Straits), and to the Indian Ocean (through the Strait of Malacca). All of these straits are shallow except the Luzon Strait whose maximum depth is 2400 m. Con-

sequently the SCS is considered a semienclosed water body (Huang et al. 1994). The complex topography includes the broad shallows of the Sunda shelf in the south/southwest; the continental shelf of the Asian landmass in the north, extending from the Gulf of Tonkin to Taiwan Strait; a deep, elliptical shaped basin in the center; and numerous reef islands and underwater plateaus scattered throughout. The shelf that extends from the Gulf of Tonkin to the Taiwan Strait is consistently near 70 m deep, and averages 150 km in width; the central deep basin is 1900 km along its major axis (northeast–southwest) and approximately 1100 km along its minor axis, and extends to over 4000 m deep. The Sunda shelf is the submerged connection between southeast Asia, Malaysia, Sumatra, Java, and Borneo and is 100 m deep in the middle; the center of the Gulf of Thailand is about 70 m deep.

The SCS is subjected to a seasonal monsoon system

Corresponding author address: Prof. Peter C. Chu, Department of Oceanography, Naval Postgraduate School, Monterey, CA 93943.
E-mail: chu@nps.navy.mil

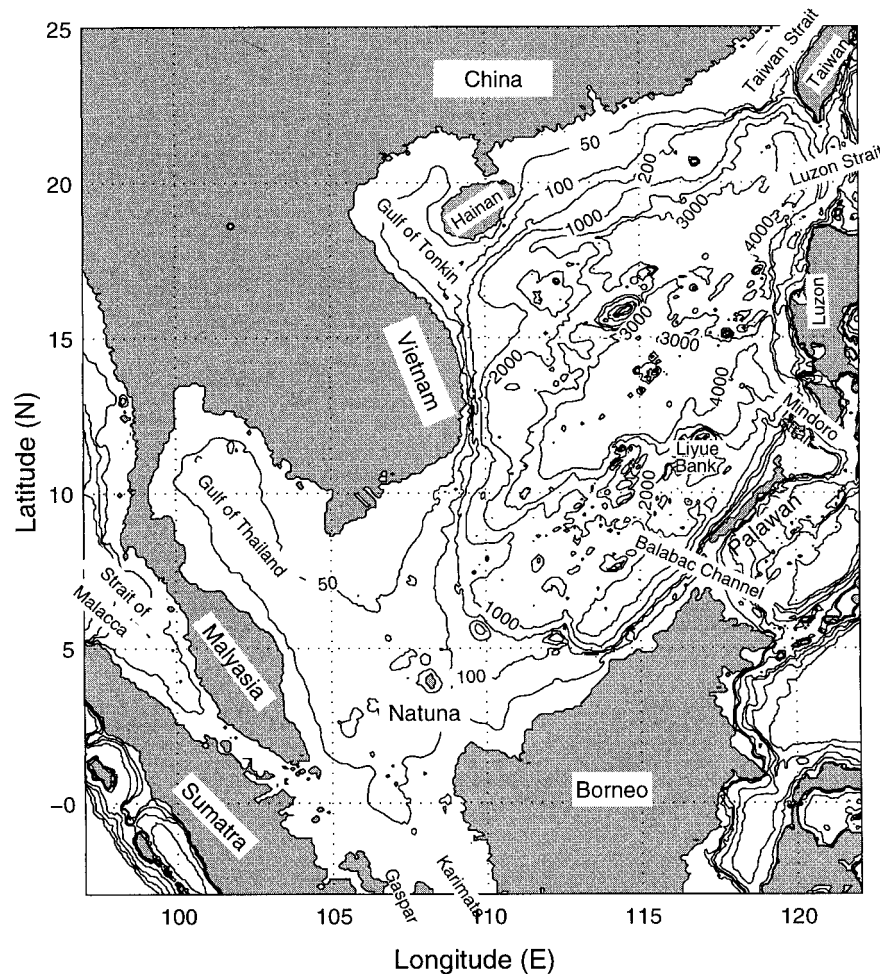


FIG. 1. Geography and isobaths showing the bathymetry (m) of the South China Sea.

(Wyrki 1961). From April to August, the weaker southwesterly summer monsoon winds result in a wind stress of over 0.1 N m^{-2} (Fig. 2a) that drives a northward coastal jet off Vietnam and anticyclonic circulation in the SCS (Fig. 3a). From November to March, the stronger northeasterly winter monsoon winds corresponds to a maximum wind stress of nearly 0.3 N m^{-2} (Fig. 2b) causing a southward coastal jet and cyclonic circulation in the SCS (Fig. 3b). The transitional periods are marked by highly variable winds and surface currents.

The observed circulation patterns of the intermediate to upper layers of the SCS are primarily forced by the local monsoon systems (Wyrki 1961), with contributions from the Kuroshio Current via Luzon Strait (or called Bashi Channel), in the southern half of the Luzon Strait. The Kuroshio enters the SCS through the southern side of the channel, then executes a tight, anticyclonic turn and exits the SCS near Taiwan. The volume transport through Luzon Strait is uncertain. Different authors reported values ranging from 8–10 Sv ($\text{Sv} \equiv 10^6 \text{ m}^3 \text{ s}^{-1}$) (Huang et al. 1994) to 3 Sv (Wyrki 1961). This flow may exert a strong influence on the properties

of the northern SCS waters. Hu and Liu (1992) believed this flow to contribute to currents in the Taiwan Strait; however, Li et al. (1996) showed that this flow did not contribute to currents in the Taiwan Strait using a numerical model.

Eddy behavior in the SCS has two distinct features. First, the number of cold eddies is far greater than the number of warm eddies and, second, the eddies are significantly affected by the bottom topography and are most likely to occur near localized high current velocity (Huang et al. 1994). Small-scale eddies with seasonal dependence have been found off coastal Vietnam in summer, near Natuna Island and in reef areas. Large-scale eddies have been found primarily during the summer monsoon (Huang et al. 1994). Based on more complete datasets such as the U.S. Navy's Master Oceanographic Observational Dataset and National Centers for Environmental Prediction monthly sea surface temperature (SST) dataset, Chu et al. (1997a, b; 1998) identified multieddy structure in the SCS.

Upwelling and downwelling occur off the coast of central Vietnam and eastern Hainan. The summer mon-

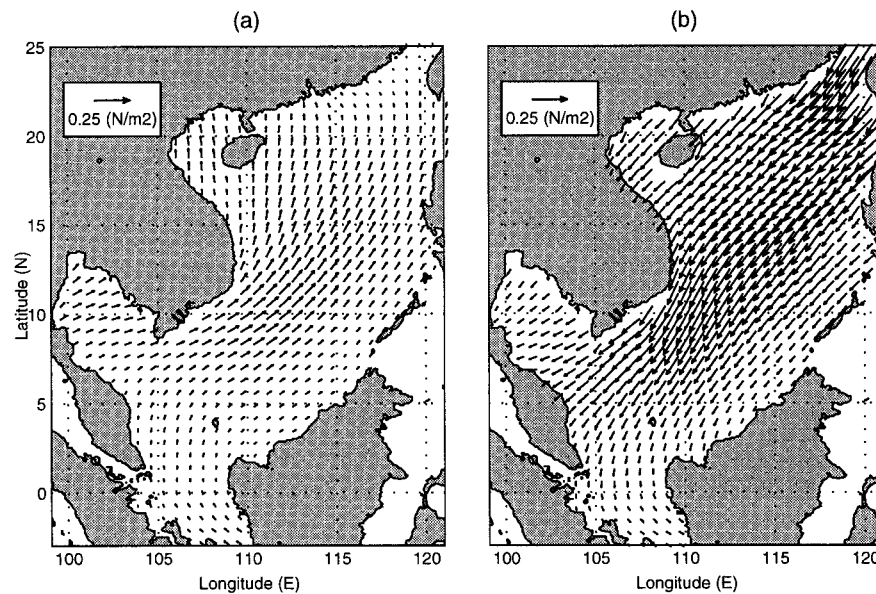


FIG. 2. Climatological wind stress for (a) Jun and (b) Dec (after Hellerman and Rosenstein 1983).

soon is believed to cause an Ekman-type drift current and corresponding offshore transport, leading to upwelling (Huang et al. 1994). Others (Chen et al. 1982) have pointed out that upwelling also occurs in these areas during winter monsoon conditions, casting doubt on previous ideas concerning the origin of these features.

In the north, the waters are cold and saline. The annual variability of salinity is small, due to the inflow and diffusion of high salinity water from the Pacific Ocean through Luzon Strait. In the south the tropical conditions cause the waters to be warmer and fresher. During the transitions the central region is alternately subjected to high and low salinity inflow as the monsoons reverse, resulting in a region of higher horizontal gradient and annual variability. Mixed layer depths vary from 30 to 40 m during the summer monsoon, and 70 to 90 m during the winter monsoon with the variation due to both wind and current (Wyrki 1961).

Three-dimensional ocean models have been used several times in the past to simulate the circulation in the SCS. Integrating a semi-implicit 12-layer shallow-water model with 50-km resolution under both mean winter and summer conditions for 15 days, Pohlmann (1987) simulated the reversal of the upper-layer circulation between the summer and winter monsoon seasons. Integrating a 23-level primitive equation model developed at Princeton University (Blumberg and Mellor 1987) with 20-km horizontal resolution under monthly mean climatological wind forcing (Hellerman and Rosenstein 1983) for a year, Chu et al. (1994) simulated the seasonal variation of the SCS circulation and Chu and Chang (1997) explained the formation of the SCS warm-core eddy in boreal spring. Integrating a global 1.5-layer re-

duced gravity model with $\frac{1}{2}$ resolution, Metzger and Hurlburt (1996) successfully simulated the upper-layer circulation and the mass exchange between the SCS, the Sulu Sea, and the Pacific Ocean.

The objective of this study is to simulate the SCS thermohaline structure, as well as the circulation, and to investigate physical processes causing seasonal variability. We used the Princeton Ocean Model (POM) to examine the mechanisms causing seasonal variation of the SCS circulation and thermal structure. The control run is designed to best simulate reality against which each experiment is compared. In the experiments, various external and internal factors are modified and the resulting circulation patterns and magnitudes compared to the control run results. Specifically we estimate the contribution (in terms of volume transport, sea surface elevation and circulation patterns) of nonlinear advection, wind forcing, and lateral boundary transport to the ocean features identified in the control results. From this we can estimate the relative importance of these factors to SCS oceanography.

2. The numerical ocean model

a. Model description

Coastal oceans and semienclosed seas are marked by extremely high spatial and temporal variability that challenge the existing predictive capabilities of numerical simulations. The POM is a time-dependent, primitive equation circulation model on a three-dimensional grid that includes realistic topography and a free surface (Blumberg and Mellor 1987). Tidal forcing was not included in this application of the model since high fre-

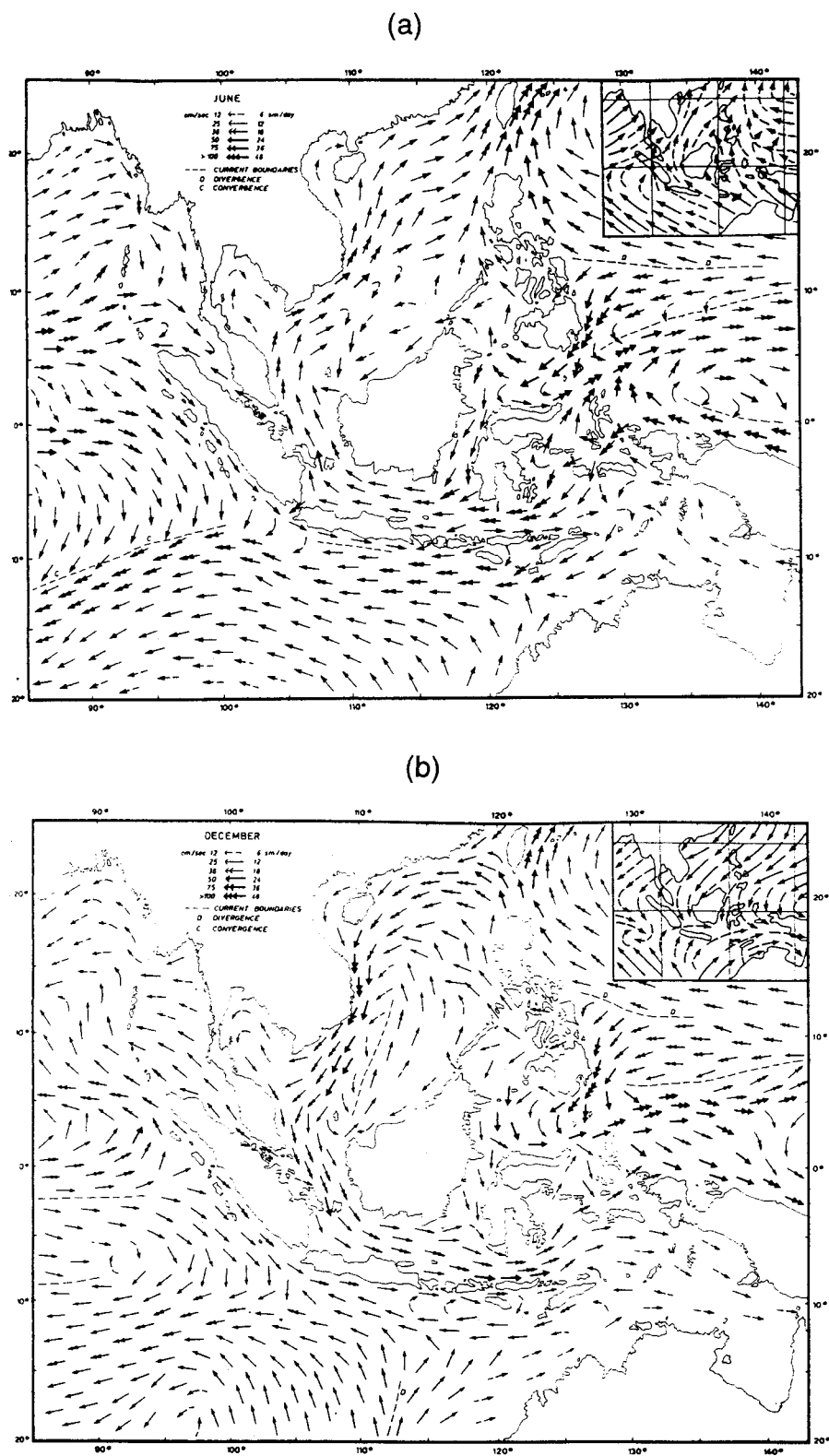


FIG. 3. Observational surface circulation: (a) Jun and (b) Dec (after Wyrtki 1961).

quency variability of the circulation is not considered. River outflow is also not included. However, the seasonal variation in sea surface height, temperature, salinity, circulation, and transport are well represented by the model. From a series of numerical experiments, the qualitative and quantitative effects of nonlinearity, wind forcing, and lateral boundary transport on the SCS are analyzed, yielding considerable insight into the external factors affecting the region oceanography. The horizontal spacing of 0.179° by 0.175° (approximately 20-km resolution) and 23 vertical sigma coordinate levels. The model domain is from 3.06°S to 25.07°N , 98.84°E to 121.16°E , which encompasses the SCS and the Gulf of Thailand, and uses realistic bathymetry data from the Naval Oceanographic Office DBDB5 database ($5'$ by $5'$ resolution). As pointed out by one of the anonymous reviewers, the DBDB5 data are inaccurate especially in shallow regions comparing to the Defense Mapping Agency (DMA) maps. We will modify the model topography files to reflect what DMA maps indicate in future studies.

Consequently, the model contains $125 \times 162 \times 23$ horizontally fixed grid points. The horizontal diffusivities are modeled using the Smagorinsky (1963) form with the coefficient chosen to be 0.2 for this application. The bottom stress τ_b is assumed to follow a quadratic law

$$\tau_b = \rho_0 C_D |\mathbf{V}_b| \mathbf{V}_b, \quad (1)$$

where ρ_0 ($=1025 \text{ kg m}^{-3}$) is the characteristic density of the sea water, \mathbf{V}_b is the horizontal component of the bottom velocity, and C_D is the drag coefficient which is specified as 0.0025 (Blumberg and Mellor 1987) in our model.

b. Atmospheric forcing

The atmospheric forcing for the SCS application of the POM includes mechanical and thermohaline forcing. The wind forcing is depicted by

$$\rho_0 K_M \left(\frac{\partial u}{\partial z}, \frac{\partial v}{\partial z} \right)_{z=0} = (\tau_{0x}, \tau_{0y}), \quad (2)$$

where (u, v) and (τ_{0x}, τ_{0y}) are the two components of the water velocity and wind stress vectors, respectively. The wind stress at each time step is interpolated from monthly mean climate wind stress (Hellerman and Rosenstein 1983), which was taken as the value at the middle of the month. The wind stress has a typical magnitude of $0.1\text{--}0.2 \text{ N m}^{-2}$ (Fig. 2). Over the two monsoon seasons the wind varies with location and time, leading to a complicated distribution of wind stress.

Surface thermal forcing is depicted by

$$K_H \frac{\partial \theta}{\partial z} = \alpha_1 \left(\frac{Q_H}{\rho C_p} \right) + \alpha_2 C (\theta_{\text{obs}} - \theta) \quad (3)$$

$$K_S \frac{\partial S}{\partial z} = \alpha_1 Q_S + \alpha_2 C (S_{\text{obs}} - S), \quad (4)$$

where θ_{obs} and S_{obs} are the observed potential temperature and salinity, C_p is the specific heat, and Q_H and Q_S are surface net heat and salinity fluxes, respectively. The relaxation coefficient C is the reciprocal of the restoring time period for a unit volume of water. The parameters (α_1, α_2) are (0, 1)-type switches: $\alpha_1 = 1, \alpha_2 = 0$, would specify only flux forcing is applied; $\alpha_1 = 0, \alpha_2 = 1$, would specify that only restoring type forcing is applied. In this study, the surface thermal forcing is determined solely by restoring forcing; that is, $\alpha_1 = 0$ and $\alpha_2 = 1$ in (3)–(4). The relaxation coefficient C is taken to be 0.7 m/day, which is equivalent to a relaxation time of 43 days for an upper layer 30 m thick (Chu et al. 1996). The net effect is to prevent any deviation from climatology and ensure that the SCS acts as a heat source. The mixing coefficients $K_M, K_H,$ and K_S were computed using a level two turbulence closure hypothesis (Mellor and Yamada 1982).

c. Lateral boundary forcing (Wyrтки type)

Closed lateral boundaries, that is, the modeled ocean bordered by land, were defined using a free-slip condition for velocity and a zero gradient condition for temperature and salinity. No advective or diffusive heat, salt, or velocity fluxes occur through these boundaries.

At open boundaries, the numerical grid ends but the fluid motion is unrestricted. Uncertainty at open boundaries makes marginal sea modeling difficult. Three approaches, local-type, inverse-type, and nested basin/coastal modeling are available for determining the open boundary condition. Here, we take the local-type approach, that is, to use the radiative boundary condition with specified volume transport. When the water flows into the model domain, temperature and salinity at the open boundary are likewise prescribed from the climatological data (Levitus 1984). When water flows out of the domain, the radiation condition was applied:

$$\frac{\partial}{\partial t}(\theta, S) + U_n \frac{\partial}{\partial n}(\theta, S) = 0, \quad (5)$$

where the subscript n is the direction normal to the boundary.

As we pointed out in the introduction, flows through SCS straits are quite uncertain. It is not an easy job to choose one among various estimations. Despite being old, Wyrтки's (1961) data provide a balanced estimation of volume transports for the Luzon Strait, Taiwan Strait, and Gasper–Karimata Strait with seasonal variations (Table 1). Since there are no reliable estimations at the Balabac Channel, Mindoro Strait, and Strait of Malacca, we assumed zero transport there. Such a treatment, especially at the Mindoro Strait, may distort the solution.

To overcome this model weakness, a logical approach is to develop a nested basin/coastal model. Lateral open boundary conditions will be obtained from the basin model output. For the moment, we may call our lateral open boundary forcing as Wyrтки-type forcing.

TABLE 1. Bimonthly variation of volume transport (Sv) at the lateral open boundaries. The positive/negative values mean outflow/inflow and were taken from Wyrski (1961).

	Month					
	Feb	Apr	Jun	Aug	Oct	Dec
Gaspar–Karimata Straits	4.4	0.0	−4.0	−3.0	1.0	4.3
Luzon Strait	−3.5	0.0	3.0	2.5	−0.6	−3.4
Taiwan Strait	−0.9	0.0	1.0	0.5	−0.4	−0.9

d. Initial conditions and initialization

The model was integrated with all three components of velocity (u , v , w) initially set to zero, and with temperature and salinity specified by interpolating climatology data (Levitus 1984) to each model grid point. The model year consists of 360 days (30 days per month), day 361 corresponds to 1 January. It was found that 90 days were sufficient for the model kinetic energy to reach quasi-steady state under the imposed conditions (Fig. 4). In order to first capture the winter monsoon to summer monsoon transition, the model was started from day 300 (30 October), and run to day 390 (30 January next year) for spinup. After day 390, the model was run another three years for each experiment.

e. Mode splitting

For computational efficiency, the mode splitting technique (Blumberg and Mellor 1987) is applied with a barotropic time step of 25 seconds, based on the Courant–Friederichs–Levy (1928) computational stability (CFL) condition and the external wave speed; and a baroclinic time step of 900 seconds, based on the CFL condition and the internal wave speed.

f. Experiment design

Our approach was to carry out four numerical experiments: one control and three sensitivity runs. All runs were completed for the same three year period encompassing both summer and winter monsoons, and, except as specified below, utilized the same initial conditions (on day 300).

Run 1 was the control run (Wyrski-type lateral open boundary forcing). The three sensitivity runs were run 2: linear dynamics, run 3: no winds, and run 4: zero lateral transport at the open boundaries. The difference between the control and the sensitivity runs at each grid point and time should then isolate the nonlinear dynamics, wind forcing effect, and lateral boundary effect, enabling independent examination of each.

The thermohaline structure, sea surface elevation, circulation patterns, and volume transport that constitute the SCS oceanography will be identified from the control run for subsequent comparative analysis. An important assumption is made that the differences are lin-

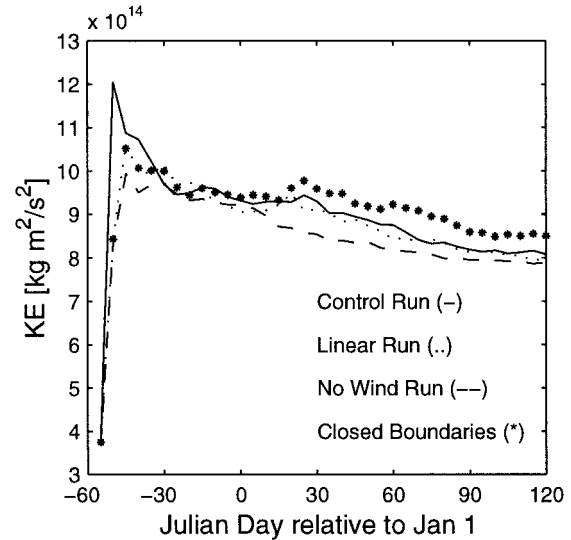


FIG. 4. Temporal variation of total kinetic energy. The model is integrated from 1 Nov and reaches quasi-steady state after 90 days of integration.

ear, that is, higher-order terms and interactions are negligible and can be ignored. This assumption will be examined and qualified.

3. The simulation (control run)

a. Circulation

The most obvious feature of both the summer and winter SCS circulation, measured and modeled, is the western boundary current, the Vietnam coastal jet (VCJ). Hinted at in Wyrski's (1961) depiction but more explicit in our model are the cross-basin currents located at 11°–14°N. The model simulates both the summer and winter SCS circulation quite well compared to the observational study (Wyrski 1961).

During the summer monsoon period (mid-May to August) winds blow from the southwest and the SCS surface circulation generally follows suit with anticyclonicity in the southern basin (Fig. 5a). Inflow is through the southern Gaspar and Karimata Straits and outflow is through the northern Taiwan Strait and eastern Luzon Strait (Table 1). The simulated summer (June–August) mean general circulation pattern has the following features. Velocities reach 1 m s^{-1} at the peak of the summer monsoon within the VCJ. The western boundary current splits into two currents at 12°N: the coastal current and the offshore current. The offshore current further bifurcates and partially leaves the coast; the bifurcation point is near the south Vietnam bight at 10°N, 110°E. The cross-basin zonal current reaches 14°N and a core speed of 0.3 m s^{-1} . The coastal branch continues north, then east at Hainan Island.

During the winter monsoon period (November to March) the winter Asian high pressure system brings

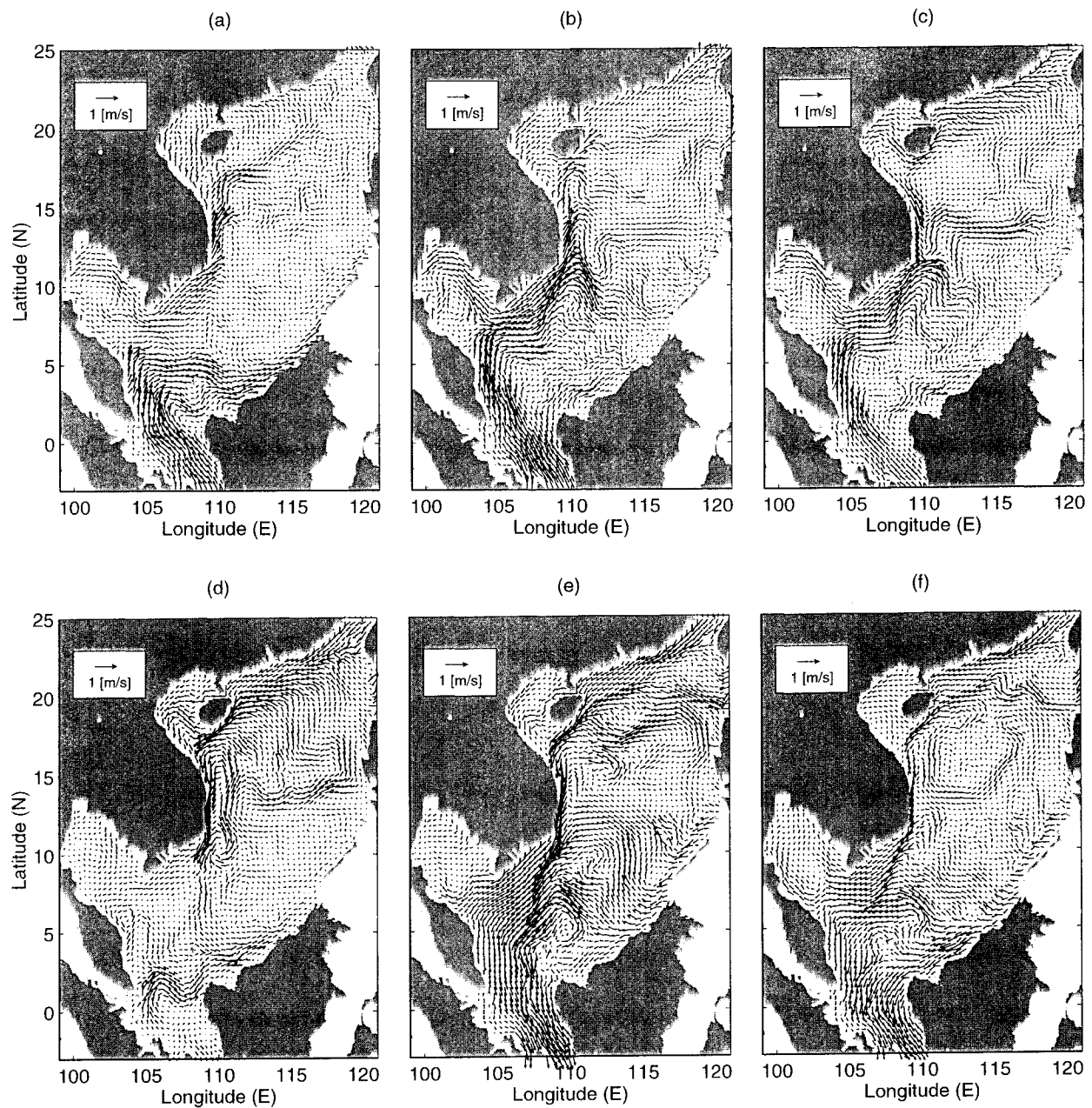


FIG. 5. Surface circulation for control run on (a) 15 May, (b) 15 Jul, (c) 15 Sep, (d) 15 Oct, (e) 15 Dec, and (f) 15 Mar.

strong winds from the northeast and the SCS surface circulation pattern is cyclonic (Figs. 5d–f). Inflow from Luzon Strait (the Kuroshio intrusion) and from the Strait of Taiwan augments currents southwestward along the Asian continental shelf, then southward along the coast of Vietnam and eventually out through the Gasper and Karimata Straits in the south. Western intensification of the general cyclonic circulation pattern was also simulated. From the south coast of Hainan Island, the current intensifies as it flows from north to south along the Vietnam coast. Average speed is around 0.8 m s^{-1} in

the core. As winter progresses, near-surface currents along the coast of Borneo begin to turn northwest, eventually flowing directly away from the coastline and into the Natuna eddy (at 5°N , 110°E) where the southern edge of the deep basin meets the Sunda shelf (Fig. 5e); the south extension of the VCJ veers westward. In early spring a northward surface current developed adjacent to the VCJ (Fig. 5f) and persists through the transition periods to the start of the summer monsoon.

The magnitude of the Ekman surface current, V_{E0} , is calculated by

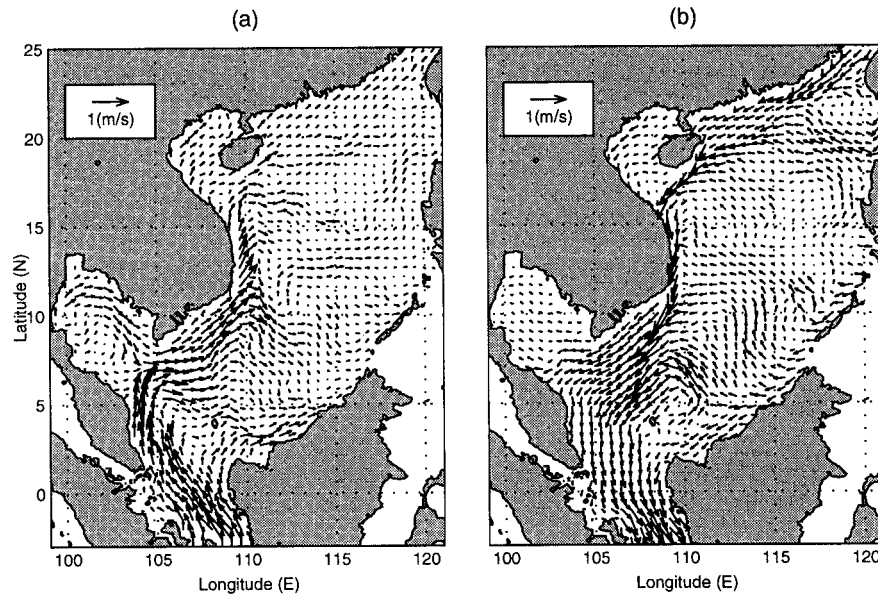


FIG. 6. Mean surface circulation for control run during (a) summer and (b) winter.

$$V_{E0} = \frac{\sqrt{2}\pi\tau}{D_E\rho_0|2\Omega\sin\phi|}, \quad (6)$$

where τ is the magnitude of the surface wind stress, Ω the angular speed of rotation of the Earth, ϕ the latitude, and D_E the Ekman layer depth. For a rough estimation on the effects of Ekman drift on the SCS surface currents, we use the following values:

$$\phi = 12^\circ, \quad D_E = 100 \text{ m}.$$

The maximum wind stress τ in the winter (summer) is 0.3 N m^{-2} (0.1 N m^{-2}). The maximum surface Ekman current is around 0.43 m s^{-1} (0.14 m s^{-1}) in the winter (summer).

In order to compare the difference of the two monsoon seasons, we averaged the model variables such as velocity, surface elevation, temperature, and salinity over the two periods: June–August (summer) and December–February (winter.) The surface circulations for the summer (Fig. 6a) show the strong VCJ flowing northward to northeastward. The winter circulations (Fig. 6b) indicate a reverse pattern: the VCJ flowing southward to southeastward. The seasonal variation of VCJ is illustrated by the zonal cross sections of v component at 13°N (Fig. 7) for winter (December–February) and summer (June–August). The summer VCJ is flowing northward with a mean maximum speed of 0.5 m s^{-1} and a width of 100 km , extending to a depth of around 200 m (Fig. 7a). The winter VCJ is a much stronger southward-flowing boundary current with a mean maximum velocity of 0.95 m s^{-1} and a width of 100 km , extending to a depth of 500 m (Fig. 7b).

Average summer sea surface elevation varies from -0.1 to 0.1 m with maximum values at the northeastern part near Luzon (Fig. 8a.). Sea surface heights for the

winter show a 0.2-m depression over the deep basin with maximum values in the southwestern part over the Sunda shelf and the Gulf of Thailand (Fig. 8b). These results are consistent with the harmonic analysis on TOPEX/Poseidon altimetry data (Yanagi et al. 1997). Figure 9 shows the cotidal and corange charts of the annual tide constituent, S_a . The amplitude of S_a is large at the northeastern and southwestern parts (Fig. 9a) and its phase differs 180° on both sides (Fig. 9b). The S_a constituent takes its maximum in August at the northeastern part and in December at the southwestern part. Thus, both numerical simulation and satellite data analysis suggest that such a surface elevation anomaly is caused by the current axis shift of the seasonal circulation and the geostrophic relation.

b. Thermohaline structure

Isotherms and isohalines for summer and winter are nearly horizontal from east to west except at the coastal regions (Fig. 10). Localized lifting of the isotherms and isohalines during summer at the west boundary indicates coastal upwelling inside the VCJ (Figs. 10a and 10c). Localized descent of the isotherms and isohalines during winter at the west boundary indicates coastal downwelling inside the VCJ (Figs. 10b and 10d). Both coastal upwelling and downwelling, combined with the high velocity shear across the VCJ, results in baroclinic instability. This mechanism may contribute to the summer bifurcation of the VCJ.

Latitudinal thermohaline variation for summer and winter is also shown in Figs. 10e–h. In general, model thermohaline structure is consistent with the two SCS water masses described by Ma (1998.) Over the southern basin there is a general lifting of isotherms of $40\text{--}50 \text{ m}$

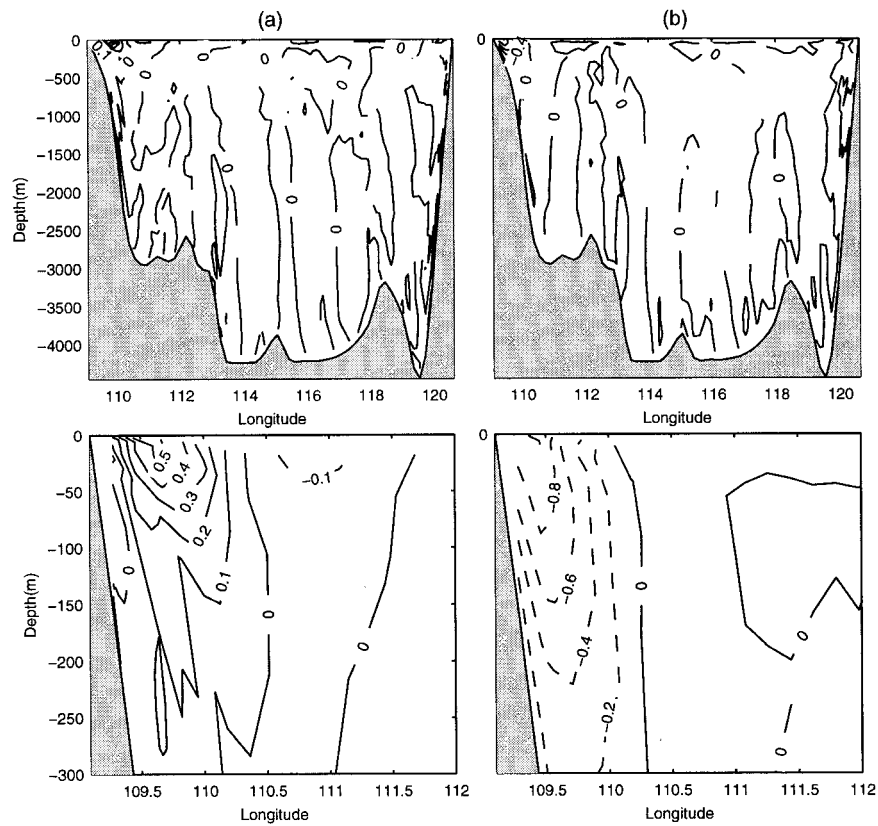


FIG. 7. Mean latitudinal velocity (m s^{-1}) for control run at the 13°N cross section during (a) winter and (b) summer. Contour interval is 0.1 m s^{-1} .

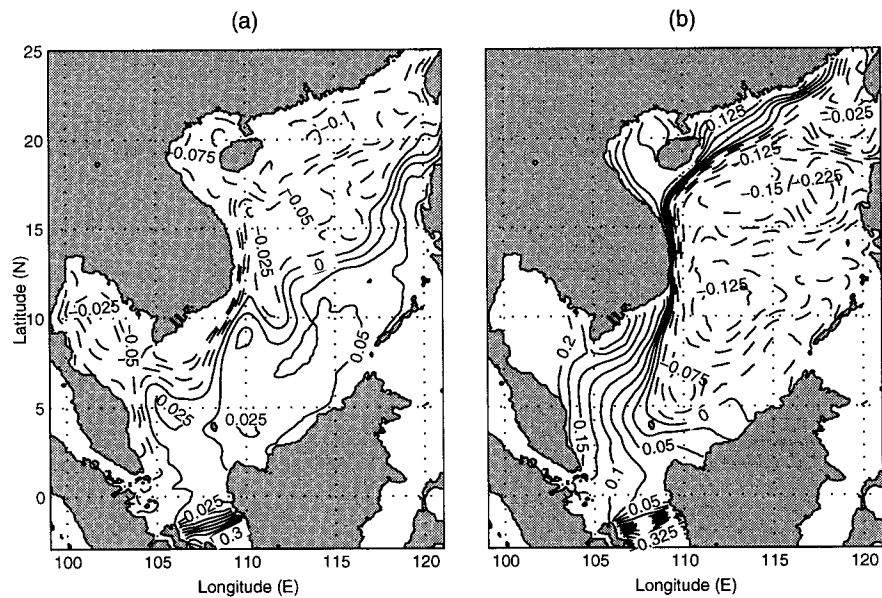


FIG. 8. Mean surface elevation (m) for control run during (a) summer and (b) winter. Contour interval is 0.025 m .

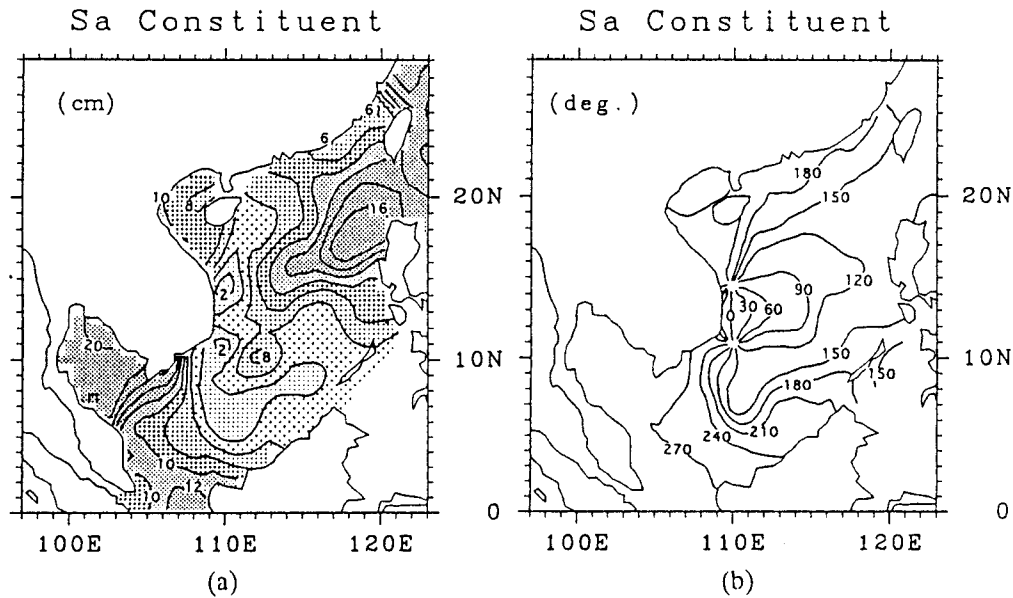


FIG. 9. Corange and cotidal charts of S_a constituent (after Yanagi et al. 1997).

from winter to summer above 200 m. In the northern SCS, near-surface waters (20–50 m) are influenced by the winter inflow of North Pacific Kuroshio water. They are uniformly colder and more saline, and there is a weaker thermocline in winter than in summer. In the south the equatorial climate and summer inflow from the shallow Java Sea cause the water mass to be fresher, warmer, and with a slightly deeper thermocline. The model SCS summer thermocline depth is in good agreement with Ma (1998), at 30 and 50 m, as opposed to the model winter depth, which is much shallower. The discrepancy in winter may be caused by using restoring type surface fluxes.

c. Volume transport

The volume transport streamfunctions for summer and winter are shown in Figs. 11a and 11b. For the SCS deep basin, the barotropic flow reveals an anticyclonic (cyclonic) gyre in the summer (winter). For the SCS continental shelf/slope regions, the volume transport has an evident seasonal variation. Winter volume transport is strongest along the north and west slope, with significant eddy and meander activity, and across the southern slope of the deep basin. Average winter VCJ transport is about 10.6 Sv. Summer shows a weaker VCJ transport (5.5 Sv) with similar transport along the southern slope of the deep basin, again with noticeable eddy activity (Table 2).

d. Natuna Island eddy

During winter, the confluence of the VCJ and the offshore flow from Borneo in the Sunda shelf generates a mesoscale cyclonic eddy (Fig. 6b), here termed the

Natuna Island eddy (NIE), consistent with observations of late winter surface cyclonic flow near Natuna Island described by Wyrki (Fig. 3b). This eddy shows little variability during the winter, with maximum swirl velocity of 0.6 m s^{-1} at the peak of the winter monsoon but no variation in position. During the summer, NIE becomes a weak anticyclonic eddy (Fig. 6a). As shown in Fig. 12, the winter NIE has an average core velocity of $0.45\text{--}0.5 \text{ m s}^{-1}$. The east–west slanted eddy core is deeper on the west side (depth ~ 40 m) of the eddy than on the east side (depth ~ 20 m). The vertical shear of horizontal velocity promotes baroclinic instability.

4. Driving mechanisms

We analyzed the results of the four experiments to identify the driving mechanisms for the SCS circulation.

a. Effects of nonlinearity (run 1 – run 2)

In the first sensitivity study the nonlinear advection terms were removed from the dynamic equations. Otherwise, the same parameters as for the control run were used. The near-surface vector velocities for the summer (Fig. 13a) and winter (Fig. 13b) illustrate the similarity to the control run results (Fig. 6), which indicates that the nonlinearity does not change the general circulation pattern. However, our computation shows that the nonlinearity causes a noticeable change in the volume transport and the strength of the western boundary currents.

Figures 14a and 15a are plots of the difference in the volume transport streamfunction ($\Delta\psi$) for the control run minus the linear run and represents nonlinear effects for summer and winter, respectively. The biggest $\Delta\psi$ during the summer (winter) season is a deep-basin dou-

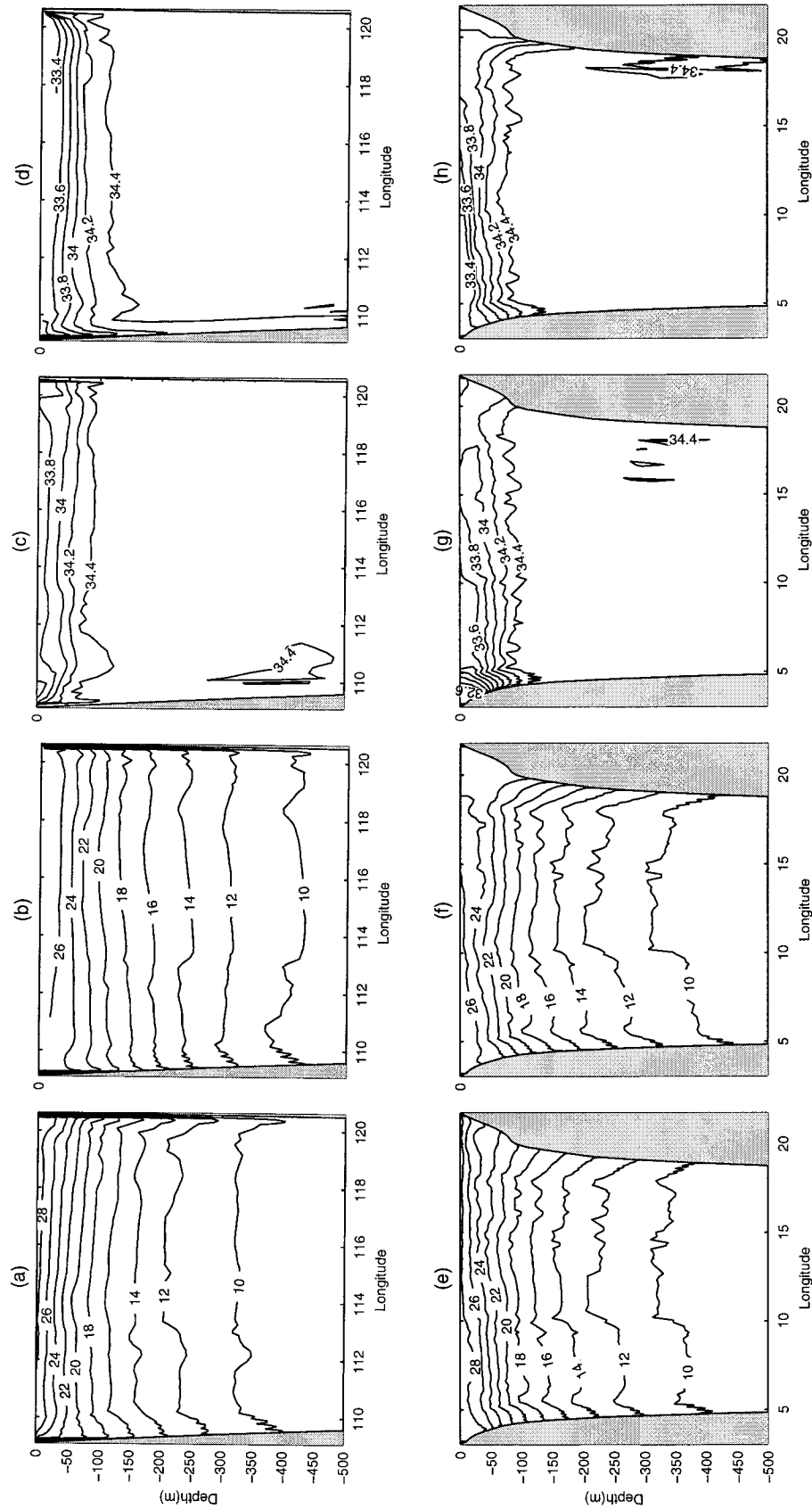


FIG. 10. Thermohaline feature simulated by the control run at the 13°N zonal cross section: (a) summer temperature (°C), (b) winter temperature (°C), (c) summer salinity (psu), (d) winter salinity (psu), and at 113°E latitudinal cross section: (e) summer temperature (°C), (f) winter temperature (°C), (g) summer salinity (psu), and (h) winter salinity (psu). Contour interval for temperature is 2°C and for salinity 0.2 psu.

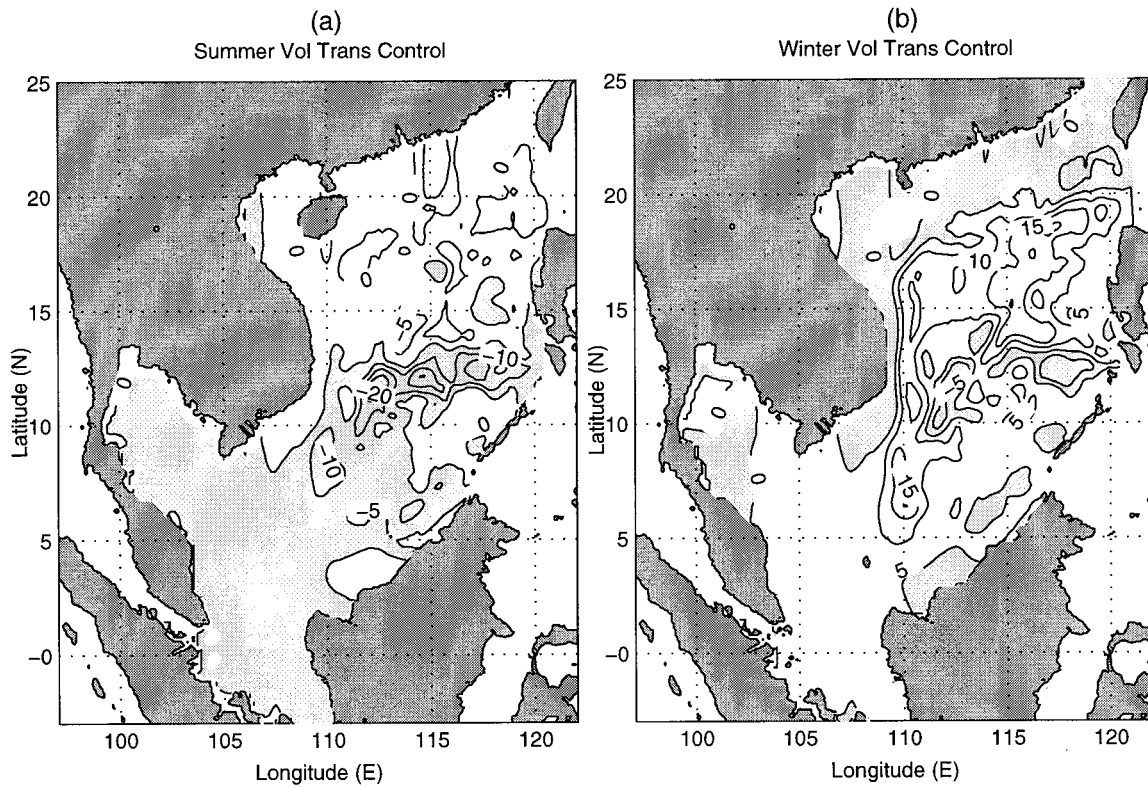


FIG. 11. Mean total volume transport streamfunction (Sv) for control run during (a) summer and (b) winter. Contour interval is 5 Sv. The shaded regions indicate negative values.

ble-gyre feature: an anticyclonic gyre with a minimum value of -4 Sv (-6 Sv) west of Luzon (16°N , 116°E) and a cyclonic gyre with a maximum value of 8 Sv (12 Sv) west of Liyue Bank (11°N , 115°E). The double-gyre structure in winter indicates (i) a westward cross-basin transport (15 Sv) near 13°N (between the two gyres), (ii) increase (decrease) of cyclonic (anticyclonic) transport in the southwestern basin (south of 13°N), and (iii) increase (decrease) of anticyclonic (cyclonic) transport in the northeastern basin (north of 13°N). Furthermore, two nearly parallel zero curves of $\Delta\psi$ show up near the Vietnam coast during the summer (Fig. 14a). One curve is close to the coast, and the other curve is offshore. This shows that $\Delta\psi = 0$ on the entire Vietnam shelf, resulting in no change in the northward VCJ transport in the summer. However, during the winter such a feature ($\Delta\psi = 0$) appears only north of 13°N , and some southward volume transport increment ($\Delta\psi = 4$ Sv) shows up near the Vietnam coast south of 13°N . After

averaging $\Delta\psi$ over the Vietnam coast shelf break, we estimated that the nonlinear advection brings a 3.1 Sv of the VCJ.

In contrast to the situation at 13°N , nonlinear effects in summer are important at 6°N . A cross section of the latitudinal velocity difference during the summer at 6°N shows that nonlinear advection augments the coastal core current at the western boundary by about 0.25 m s^{-1} and is responsible for offshore eddy activity (Fig. 16a). Such a nonlinear effect was also found in the surface velocity vector difference ($\Delta\mathbf{V}$) field. For both seasons, the nonlinear effect on circulation is very weak in the deep SCS basin and quite evident near the west coast and southern shelf regions (Figs. 17a and 18a). The nonlinear effect is essential for the NIE formation near 110°E , 6°N (Fig. 18a).

b. Wind-induced circulation (run 1 – run 3)

The difference between Run 1 and Run 3 shows the monsoon wind effects on the SCS surface circulation and SST for summer and winter respectively. The feature of the summer wind effect (Fig. 17b) on circulation and volume transport is in contrast to the winter wind forcing (Fig. 18b). The winter wind forcing causes the cyclonic gyre northeast Natuna Island (the NIE) with an average 0.3 – 0.4 m s^{-1} rotational velocity, the cross-

TABLE 2. Volume transport (Sv) of individual features simulated by the control run.

Feature	Transport
Summer Vietnam coastal jet	5.5
Winter Vietnam coastal jet	10.6
Natuna Island eddy	5.0

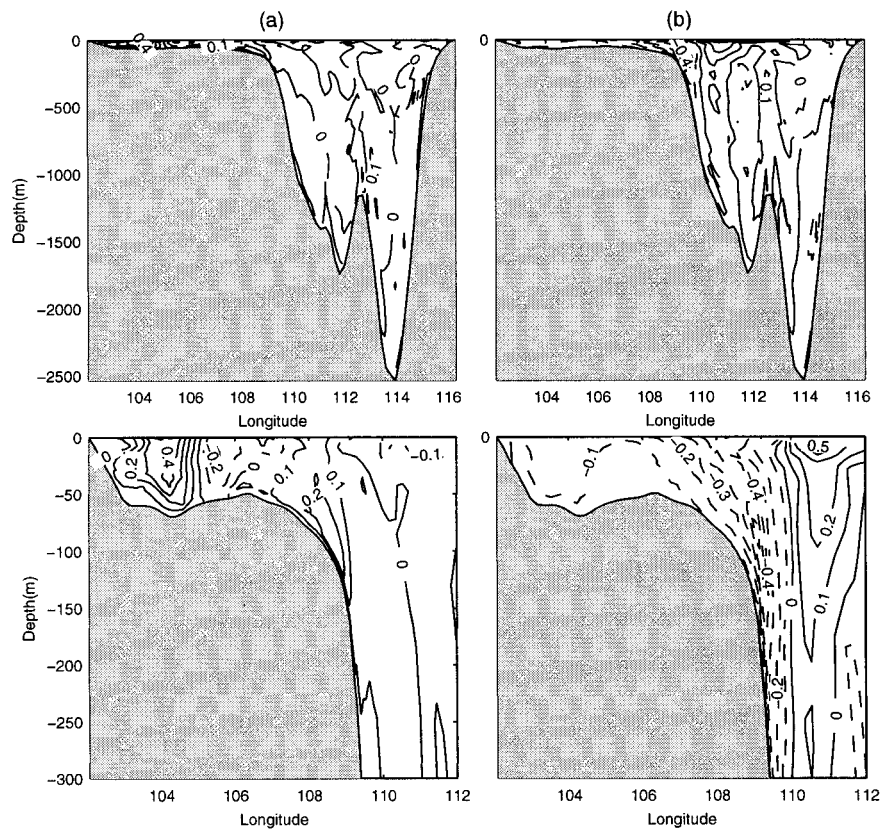


FIG. 12. Mean latitudinal velocity for control run at the 6°N cross section during (a) summer and (b) winter. Contour interval is 0.1 m s⁻¹.

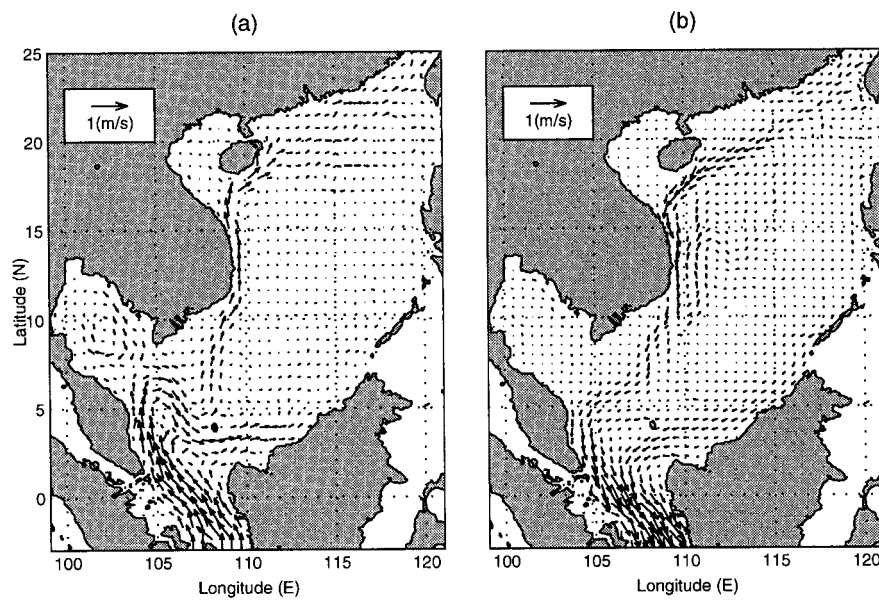


FIG. 13. Mean surface circulation for linear run during (a) summer and (b) winter.

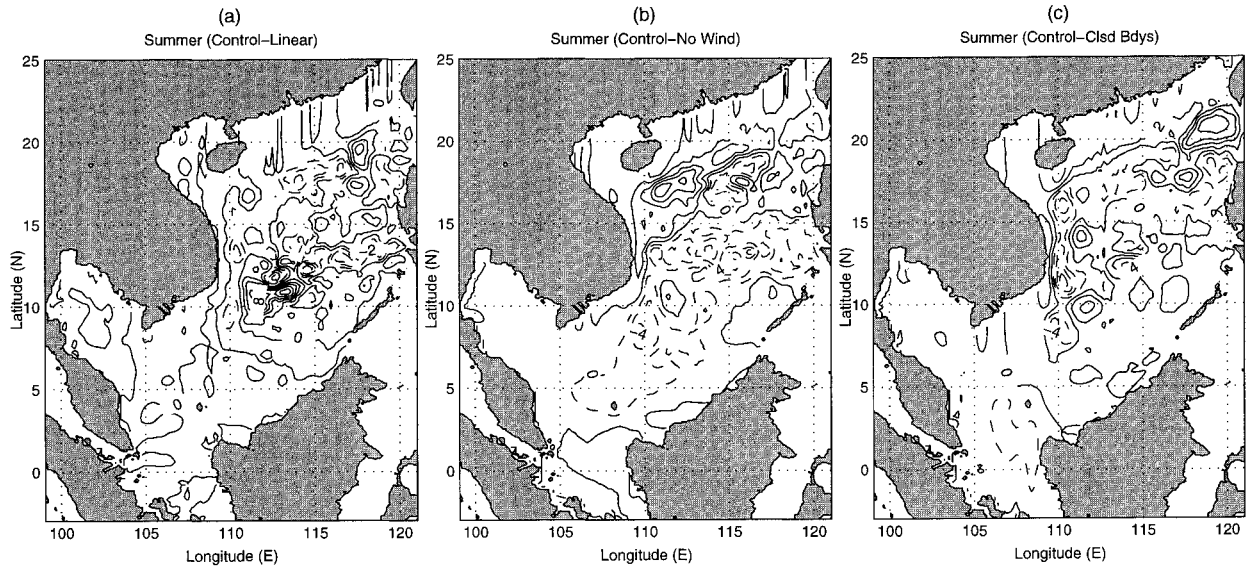


FIG. 14. Summer volume transport anomaly (Sv) caused by effects of (a) nonlinearity, (b) winds, and (c) boundary forcing. Contour interval is 2 Sv.

basin flow and connecting loop across the Sunda shelf around Natuna Island. The winter VCJ flows with $0.3\text{--}0.4\text{ m s}^{-1}$ velocity (Fig. 18b), corresponding to a southward volume transport of 4.6 Sv (Fig. 15b). The China slope flow is actually slightly more than in the control run. When winds are removed from the forcing, the model results show considerable change in the structure of the summer circulation and a virtual disappearance of features in the winter circulation (note similarities in Figs. 6b and 18b); surface velocities are reduced by $0.20\text{--}0.3\text{ m s}^{-1}$.

The summer winds drive a mesoscale anticyclonic eddy near a shallow depression in the Sunda shelf and Natuna Island, with rotation speeds of $0.15\text{--}0.2\text{ m s}^{-1}$ (Fig. 16b.) Winds also induce the loop current joining the Sunda shelf flow and the VCJ, bifurcation of the coastal current, and cross-basin flow (Fig. 17b.) The corresponding wind effect on summer volume transport is largely limited to the northern SCS (Fig. 14b) with a $6\text{--}8\text{ Sv}$ maximum transport along the China slope and a $4\text{--}6\text{ Sv}$ eastward transport centered on 13°N , a region of significant nonlinear effect.

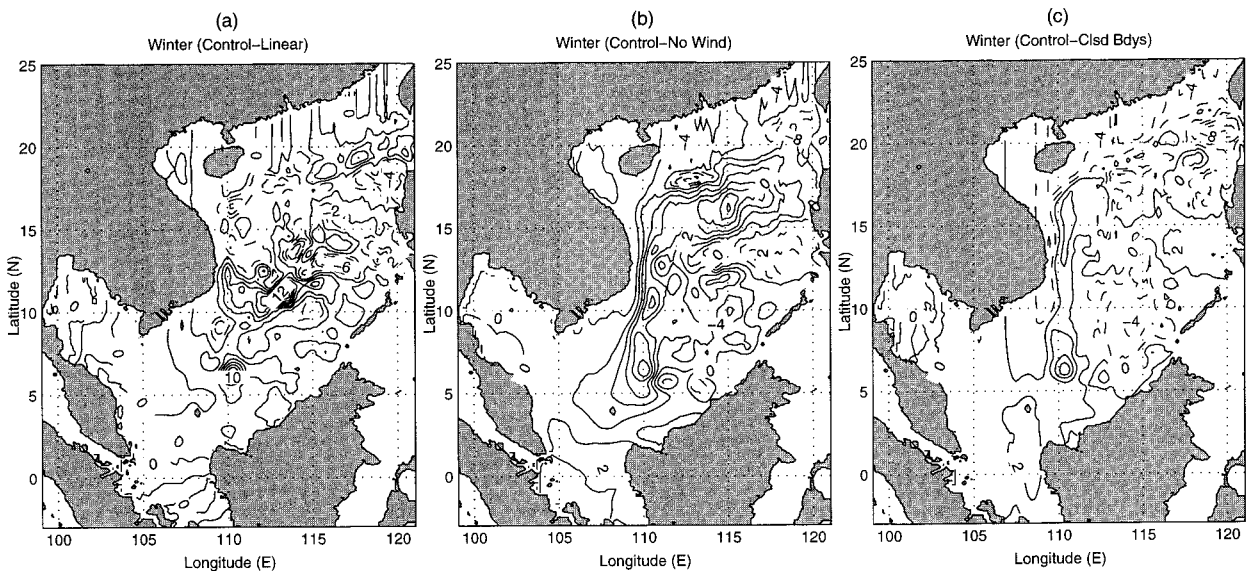


FIG. 15. Winter volume transport anomaly (Sv) caused by effects of (a) nonlinearity, (b) winds, and (c) boundary forcing. Contour interval is 2 Sv.

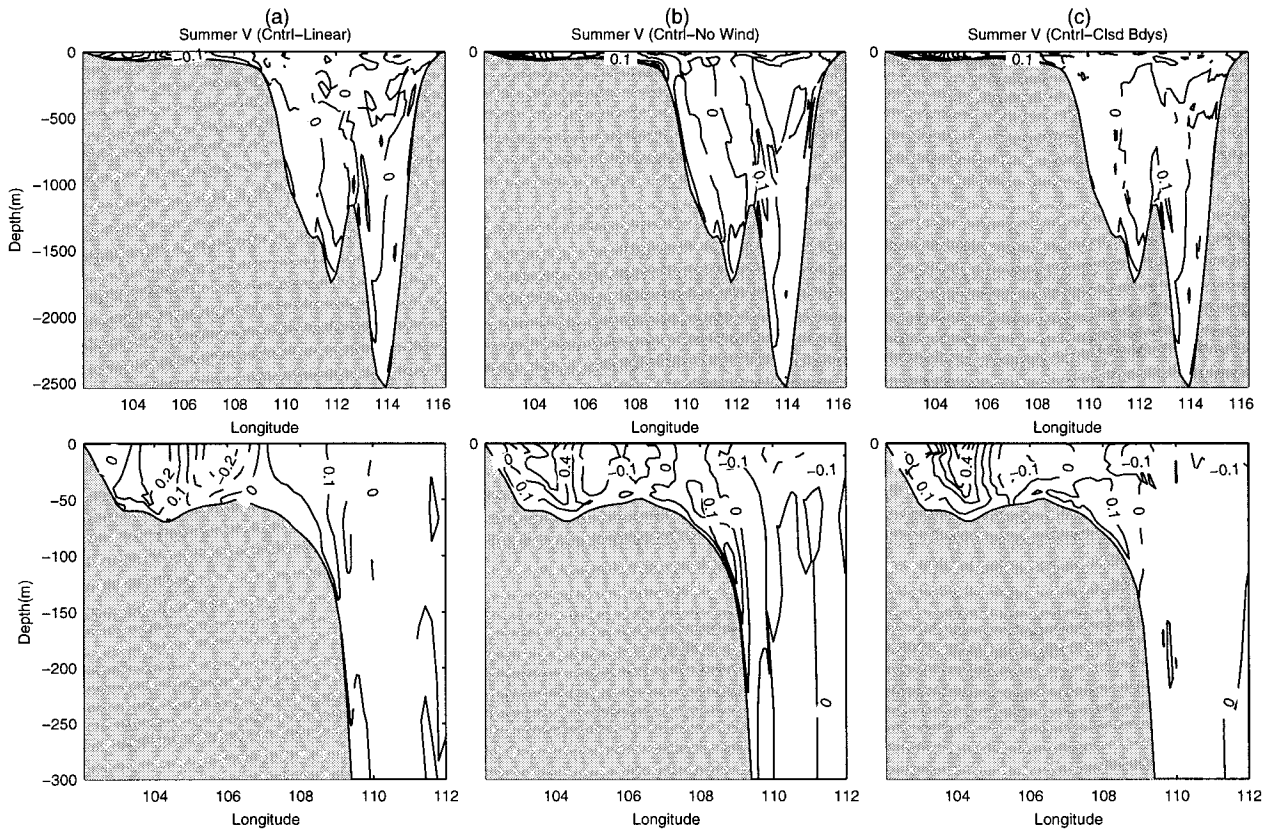


FIG. 16. Summer latitudinal velocity anomaly (m s^{-1}) at the 6°N cross section and the west coast zoomed view, caused by effects of (a) nonlinearity, (b) winds, and (c) boundary forcing. Positive (negative) values indicate northward (southward) flow; contour interval is 0.1 m s^{-1} .

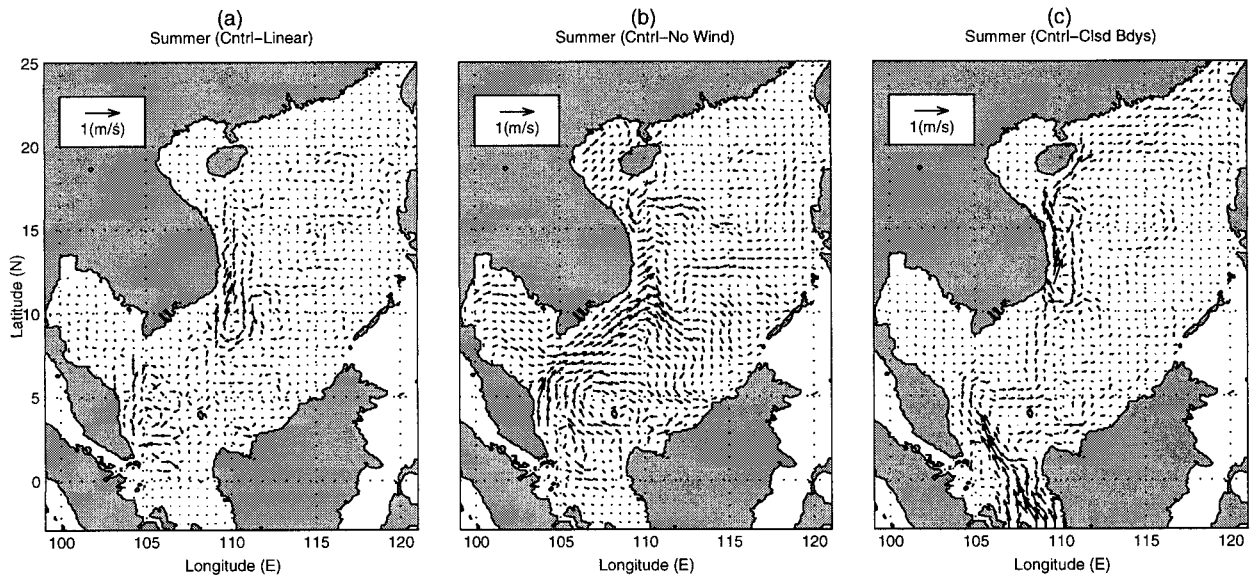


FIG. 17. Summer surface current anomaly caused by effects of (a) nonlinearity, (b) winds, and (c) boundary forcing.

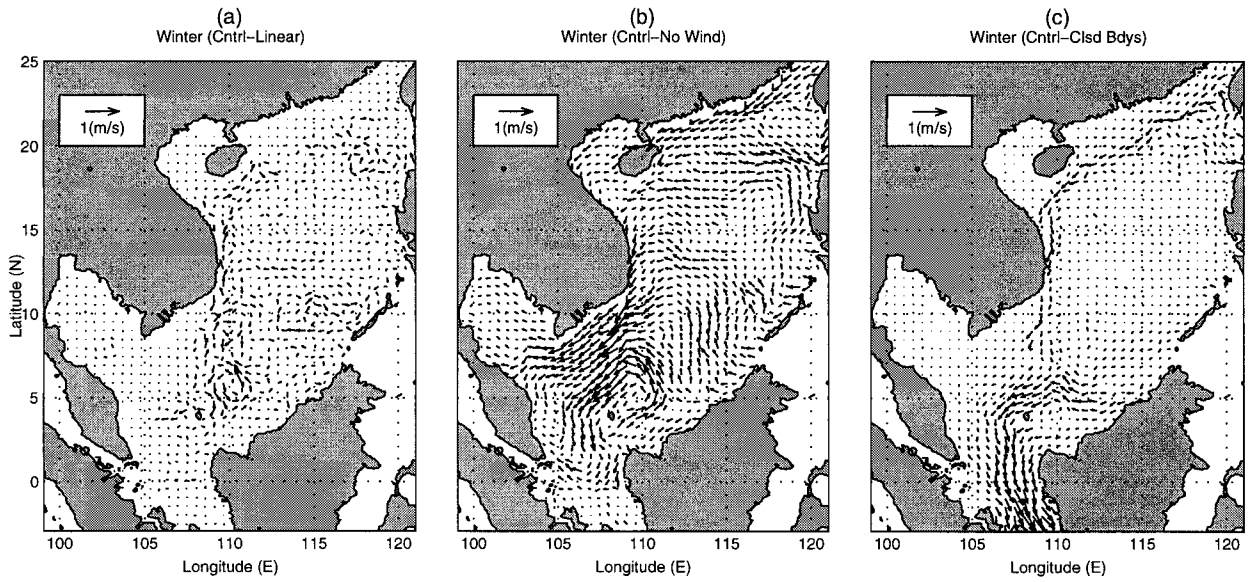


FIG. 18. As in Fig. 17 but for the winter surface current anomaly.

Summer wind reduces SST slightly (1° – 2° C) from upwelling off central and northern Vietnam and the east coast of Hainan (Fig. 19a). Winter wind decreases surface temperature to a lesser extent on the east side of the basin along the Palawan Trough (Fig. 19b).

Summer winds shift the average surface elevation to the north, increasing the elevation 5–10 cm, while elsewhere decreasing the height by the same magnitude (Fig. 20a). The winter wind increases the surface elevation over the continental shelves by 0.15–0.18 m, and decreases the elevation over the deep basin (Fig. 21a).

c. Inflow/outflow induced circulation (run 1 – run 4)

The third sensitivity study used the control run equations and forcing but closed all open lateral boundaries, preventing transport of mass, heat, or salinity through the Luzon Strait, Taiwan Strait, or Gasper and Karimata Straits. With no inflow or outflow the summer anticyclonic gyre and winter cyclonic gyre are more pronounced. Increased recirculation generally leads to greater horizontal and vertical variability of the current structure.

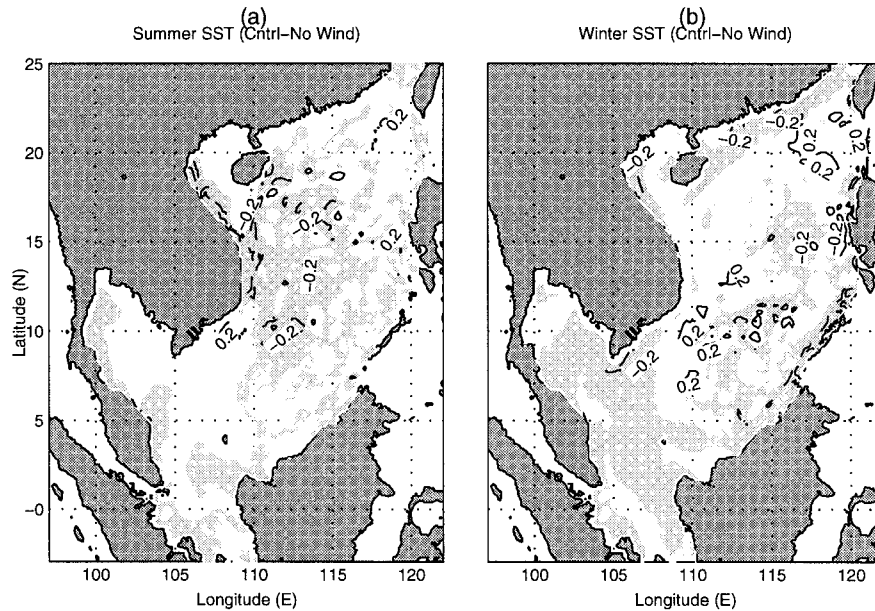


FIG. 19. Sea surface temperature anomaly caused by wind effect. Contour interval is 0.1° C; the shaded regions indicate negative values.

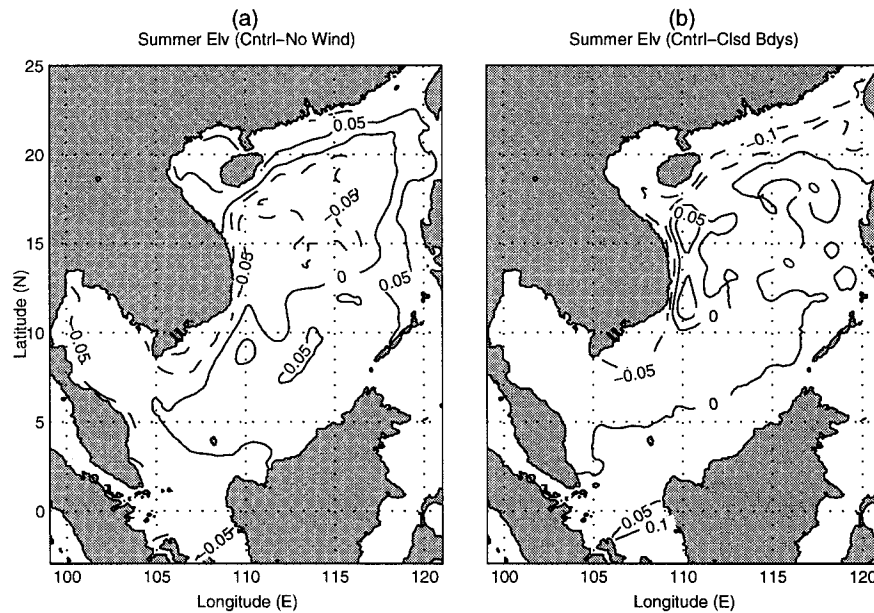


FIG. 20. Summer surface elevation anomaly (m) caused by effects of (a) winds, and (b) boundary forcing. Contour interval is 0.05 m.

The results for summer lateral boundary forcing retain more of the anticyclonic nature of the circulation than do those from wind forcing; see volume transport streamfunction difference $\Delta\psi$ (Figs. 14b,c). The flow generally hugs the slope. The largest gradient of $\Delta\psi$ is located off the south Vietnam coast (Fig. 14c), causing the strong western boundary currents. The southern inflow splits south of Natuna Island and fans across the Sunda shelf, forming a small anticyclonic eddy col-

located with that forced by the summer wind. The VCJ transports 5.5 Sv and is accompanied by a countercurrent nearby. At 6°N (Fig. 16c), however, notice that the average northward velocity throughout most of the shallow shelf region shows no discernible pattern of change, while the shelf current along the 100 m isobath decreases by 0.05–0.1 m s⁻¹. The summer circulation patterns change dramatically when the lateral boundary transport is removed. This can be seen from the surface

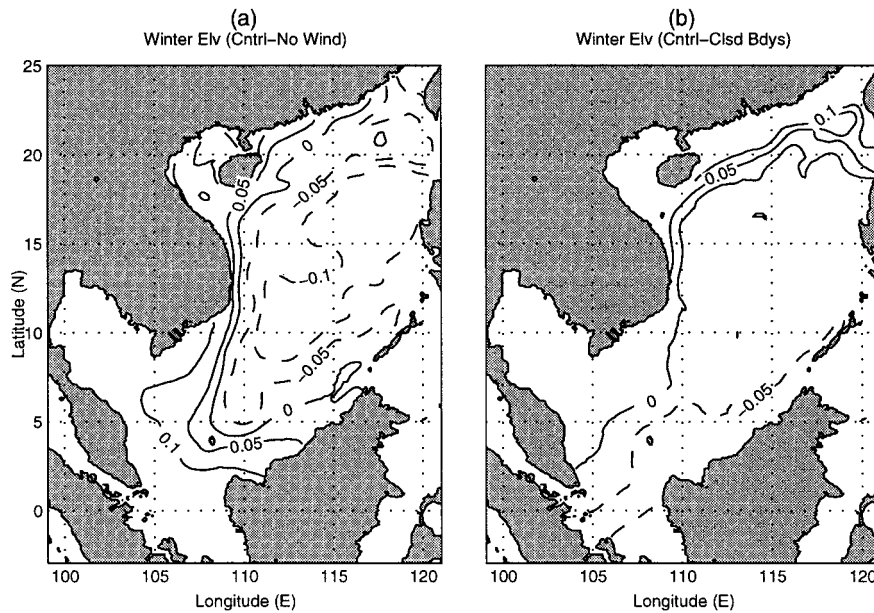


FIG. 21. Winter surface elevation anomaly (m) caused by effects of (a) winds, and (b) boundary forcing. Contour interval is 0.05 m.

velocity vector difference $\Delta \mathbf{V}$ (Fig. 17c). There is still western intensification of the current along the coast of Malaysia, and it still joins the flow out of the Gulf of Thailand to contribute to an intensification of current off southern Vietnam.

Winter closed boundary circulation patterns, on the other hand, show less difference in structure from the control run but more variability in magnitude. There is an average decrease of $0.1\text{--}0.4\text{ m s}^{-1}$ in current speed of the winter VCJ, which equates to $4\text{--}6\text{ Sv}$ southward volume transport (Fig. 15c). The Kuroshio intrusion and inflow through Taiwan Strait are obviously supplemented by recirculation flow from along the coast of Luzon Island. Near Natuna Island it is noteworthy that the structure of cross-basin circulation and current flow away from the Borneo coast are unchanged. Similarly, it is apparent that the spatial extent and shape of the gyre northeast of Natuna Island is unchanged by closing the boundary flow. In cross section, however, it can be seen that the NIE does lose some of its velocity—there is a $0.1\text{--}0.3\text{ m s}^{-1}$ decrease in the average core velocity on the western side at 6°N in this run corresponding to a volume transport of 3 Sv , associated with the decrease in velocity of the VCJ. The difference in velocity is much smaller on the eastern side, suggesting that some other effect dominates the current structure in that region.

The summer lateral boundary transport decreases the average surface elevation over the China–Vietnam continental shelf by $0.05\text{--}0.15\text{ m}$, while elsewhere increases the height with a maximum accretion of $0.2\text{--}0.4\text{ m}$ near the Karimata Strait (Fig. 20b). The winter lateral boundary transport increases the average surface elevation over the China–Vietnam continental shelf by $0.05\text{--}0.2\text{ m}$, while elsewhere decreases the height with a maximum reduction of 0.25 m near the Karimata Strait (Fig. 21b).

5. Conclusions

1) The SCS circulation and thermohaline structure was simulated in this study by the POM model under the climatological forcing. During the summer (winter) monsoon period the SCS surface circulation is generally anticyclonic (cyclonic) with a strong western boundary current (width around 100 km)—the Vietnam coastal jet. This jet has a strong seasonal variation and flows northward (southward) during summer (winter) with a mean maximum speed of 0.5 m s^{-1} (0.95 m s^{-1}), with a mean volume transport of 5.5 Sv (10.6 Sv) extending to a depth of around 200 m (500 m). During summer, the western boundary current splits and partially leaves the coast; the bifurcation point is at 14°N in May and shifts south to 10°N in July. The cross-basin zonal current reaches 12°N and a core speed of 0.6 m s^{-1} by the end of the summer. The coastal branch continues north, then east at Hainan Island. Average summer sea surface elevation varies from -0.1 to 0.1 m with maximum

values at northeastern part near Luzon. Sea surface heights for the winter show a 0.2-m depression over the deep basin with maximum values in the southwestern part over the Sunda shelf and the Gulf of Thailand. This suggests that the southwest monsoon wind in boreal summer piles up the water at the northeastern part near Luzon and the northeast monsoon wind in boreal winter piles up the water at the southwestern part over the Sunda shelf and the Gulf of Thailand. The POM model also successfully simulates a mesoscale eddy in the Sunda shelf, namely the Natuna Island eddy. This eddy is cyclonic (anticyclonic) with maximum swirl velocity of 0.6 m s^{-1} at the peak of the winter (summer) monsoon.

Isotherms and isohalines for summer and winter are nearly horizontal from east to west except at the coastal regions. Coastal upwelling and downwelling are also simulated: localized lifting (descending) of the isotherms and isohalines during summer (winter) at the west boundary. Both coastal upwelling and downwelling (causing horizontal thermohaline gradient), combined with the high velocity shear across the coastal jet, results in baroclinic instability. This mechanism may contribute to the summer jet bifurcation. In general model thermohaline structure is consistent with the two SCS water masses described by Wyrтки (1961.) Over the southern basin there is a general lifting of isotherms of $40\text{--}50\text{ m}$ from winter to summer above 200 m . In the northern SCS, near-surface waters ($20\text{--}50\text{ m}$) are influenced by the winter inflow of North Pacific Kuroshio water.

2) The model wind effects on the SCS are more pervasive than those of nonlinear dynamic effects. Similar to nonlinear effects there are areas of anticyclonic volume transport midbasin in the summer and winter, although the midbasin surface currents reverse. Summer wind effects on transport are generally divided along the axis of the monsoon wind, SW–NE, with anticyclonicity and positive elevation in the southeast and cyclonic transport and negative elevation in the northwest. The winter wind effect is largely cyclonic, including a center (with a strong surface current signature) for the NIE, with a matching steeper depression in surface elevation.

3) The model boundary forcing effect on volume transport is most easily distinguished as anticyclonic in the summer and cyclonic in the winter. The stronger transport centers of both seasons have strong surface current signatures including the NIE. Topographically linked eddy flow and transport is evident in the summer, while winter flow narrowly follows the 200-m isobath until it encounters the Sunda shelf and Natuna Island.

In the summer, SCS volume transport is mostly due to boundary forcing. Surface movement is marginally dominated by wind forcing, when the boundary-forcing surface effect (away from the southern boundary) coalesces with associated volume transport. Winds drive the offshore summer bifurcation of the VCJ. The anticyclonic gyre south of Hainan is a surface phenomena

driven by boundary flow interaction with topography and nonlinear dynamics.

In the winter, surface movement due to boundary forcing is largely limited to the perimeter of the SCS basin, specifically a narrow swath over the 200-m isobath, away from the southern boundary. Surface flow and volume transport are dominated by the wind effect except at the NIE, a mesoscale feature that must be qualified by nonlinear dynamics. Also to be qualified by nonlinear dynamics is cross-basin transport for both seasons.

4) Future studies should concentrate on less simplistic scenarios. Realistic lateral transport (especially at the Mindoro and Karimata Straits) and surface heat and salt fluxes should be included, and the use of extrapolated climatological winds needs to be upgraded to incorporate synoptic winds to improve realism. Finally, the assumption of quasi linearity that allowed us to use simple difference to quantify the effect of external forcing needs to be rigorously tested. It is very important to develop a thorough methodology to perform sensitivity studies under the highly nonlinear conditions that may exist in the littoral environment.

Acknowledgments. The authors wish to thank George Mellor and Tal Ezer of the Princeton University for most kindly proving us with a copy of the POM code and to thank Laura Ehret for programming assistance. This work was funded by the Office of Naval Research NOMP Program, the Naval Oceanographic Office, and the Naval Postgraduate School.

REFERENCES

- Blumberg, A., and G. Mellor, 1987: A description of a three-dimensional coastal ocean circulation model. *Three-Dimensional Coastal Ocean Models*, N. S. Heaps, Ed., Amer. Geophys. Union, 1–16.
- Chen, J., Z. Fu, and F. Li, 1982: A study of upwelling over Minnan-Taiwan shoal fishing ground. *Taiwan Strait*, **1**, 5–13.
- Chu, P. C., and C. P. Chang, 1997: South China Sea warm pool in boreal spring. *Adv. Atmos. Sci.*, **14**, 195–206.
- , C. C. Li, D. S. Ko, and C. N. K. Mooers, 1994: Response of the South China Sea to seasonal monsoon forcing. *Proc. Second Int. Conf. on Air–Sea Interaction and Meteorology and Oceanography of the Coastal Zone*, Lisbon, Portugal, Amer. Meteor. Soc., 214–215.
- , M. Huang, and E. Fu, 1996: Formation of the South China Sea warm core eddy in boreal spring. *Proc. Eighth Conf. on Air–Sea Interaction*, Atlanta, GA, Amer. Meteor. Soc., 155–159.
- , H.-C. Tseng, C. P. Chang, and J. M. Chen, 1997a: South China Sea warm pool detected in spring from the Navy's Master Oceanographic Observational Data Set (MOODS). *J. Geophys. Res.*, **102**, 15 761–15 771.
- , S.-H. Lu, and Y.-C. Chen, 1997b: Temporal and spatial variabilities of the South China Sea surface temperature anomaly. *J. Geophys. Res.*, **102**, 20 937–20 955.
- , C. W. Fan, C. J. Lozano, and J. L. Kirling, 1998: An airborne expandable bathythermograph survey of the South China Sea, May 1995. *J. Geophys. Res.*, **103**, 21 637–21 652.
- Courant, R., K. O. Friedrichs, and H. Levy, 1928: Uber die partiellen differenzgleichungen der mathematischen physik. *Math. Ann.*, **100**, 32–74.
- Hellerman, S., and M. Rosenstein, 1983: Normal monthly wind stress over the world ocean with error estimates. *J. Phys. Oceanogr.*, **13**, 1093–1104.
- Hu, J., and M. Liu, 1992: The current structure during summer in southern Taiwan Strait (in Chinese). *Tropic Oceanology*, **11**, 42–47.
- Huang, Q. Z., W. Z. Wang, Y. S. Li, and C. W. Li, 1994: Current characteristics of the South China Sea. *Oceanology of China Seas*, Z. Di, L. Yuan-Bo, and Z. Cheng-Kui, Eds., Kluwer, 39–46.
- Levitus, S., 1984: *Climatological Atlas of the World Ocean*, NOAA Prof. Paper No. 13, U.S. Gov. Printing Office, 173 pp.
- Li, R.-F., D.-J. Guo, and Q.-C. Zeng, 1996: Numerical simulation of interrelation between the Kuroshio and the current of the northern South China Sea. *Prog. Natural Sci.*, **6**, 325–332.
- Ma, B.-B., 1998: The South China Sea thermohaline structure and circulation. Masters thesis, Naval Postgraduate School, Monterey, California, 254 pp.
- Mellor, G., and T. Yamada, 1982: Development of a turbulence closure model for geophysical fluid problems. *Rev. Geophys. Space Phys.*, **20**, 851–875.
- , and T. Ezer, 1991: A Gulf Stream model and an altimetry assimilation scheme. *J. Geophys. Res.*, **96**, 8779–8795.
- Metzger, E. J., and H. Hurlburt, 1996: Coupled dynamics of the South China Sea, the Sulu Sea, and the Pacific Ocean. *J. Geophys. Res.*, **101**, 12 331–12 352.
- Oey, L., and P. Chen, 1991: Frontal waves upstream of a diabatic blocking: A model study. *J. Geophys. Res.*, **21**, 1643–1663.
- Pohlmann, T., 1987: A three-dimensional circulation model of the South China Sea. *Three-Dimensional Models of Marine and Estuarine Dynamics*, J. Nihoul and B. Jamart, Eds., Elsevier Science, 245–268.
- Smagorinsky, J., 1963: General circulation experiments with the primitive equations, I. The basic experiment. *Mon. Wea. Rev.*, **91**, 99–164.
- Wyrtki, K., 1961: Scientific results of marine investigations of the South China Sea and the Gulf of Thailand 1959–1961. *Naga Report*, Vol. 2, University of California at San Diego, 164–169.
- Yanagi, T., T. Takao, and A. Morimoto, 1997: Co-tidal and co-range charts in the South China Sea derived from satellite altimetry data. *La mer*, **35**, 85–93.

Statement of Ownership, Management, and Circulation

1. Publication Title Journal of Physical Oceanography	2. Publication Number		3. Filing Date
	0	0 2 2 _ 3 6 7 0	August 17, 1999
4. Issue Frequency Monthly	5. Number of Issues Published Annually 12		6. Annual Subscription Price \$55.00 Members \$405.00 Non-Members
7. Complete Mailing Address of Known Office of Publication (Not printer) (Street, city, county, state, and ZIP+4) 45 Beacon Street, Boston, Suffolk, Mass. 02108-3693			Contact Person Mary McMahon Telephone 617-227-2426 x 218

8. Complete Mailing Address of Headquarters or General Business Office of Publisher (Not printer)

45 Beacon Street, Boston, Mass. 02108-3693

9. Full Names and Complete Mailing Addresses of Publisher, Editor, and Managing Editor (Do not leave blank)

Publisher (Name and complete mailing address)
American Meteorological Society, 45 Beacon Street, Boston, Mass. 02108-3693

Editor (Name and complete mailing address)
Prof. Julian P. McCreary, Jr., University of Hawaii, 1000 Pope Road, MSB 222
Honolulu, Hawaii 96822

Managing Editor (Name and complete mailing address)
Dr. Ronald D. McPherson, American Meteorological Society
45 Beacon Street, Boston, Mass. 02108-3693

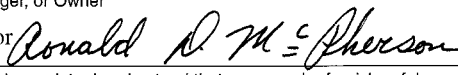
10. Owner (Do not leave blank. If the publication is owned by a corporation, give the name and address of the corporation immediately followed by the names and addresses of all stockholders owning or holding 1 percent or more of the total amount of stock. If not owned by a corporation, give the names and addresses of the individual owners. If owned by a partnership or other unincorporated firm, give its name and address as well as those of each individual owner. If the publication is published by a nonprofit organization, give its name and address.)

Full Name	Complete Mailing Address
American Meteorological Society	45 Beacon Street, Boston, Mass. 02108-3693

11. Known Bondholders, Mortgagees, and Other Security Holders Owning or Holding 1 Percent or More of Total Amount of Bonds, Mortgages, or Other Securities. If none, check box None

Full Name	Complete Mailing Address

12. Tax Status (For completion by nonprofit organizations authorized to mail at nonprofit rates) (Check one)
The purpose, function, and nonprofit status of this organization and the exempt status for federal income tax purposes:
 Has Not Changed During Preceding 12 Months
 Has Changed During Preceding 12 Months (Publisher must submit explanation of change with this statement)

13. Publication Title Journal of Physical Oceanography		14. Issue Date for Circulation Data Below June 1999	
15. Extent and Nature of Circulation		Average No. Copies Each Issue During Preceding 12 Months	No. Copies of Single Issue Published Nearest to Filing Date
a. Total Number of Copies (<i>Net press run</i>)		1800	1700
b. Paid and/or Requested Circulation	(1) Paid/Requested Outside-County Mail Subscriptions Stated on Form 3541. (<i>Include advertiser's proof and exchange copies</i>)	1116	1073
	(2) Paid In-County Subscriptions (<i>Include advertiser's proof and exchange copies</i>)	0	0
	(3) Sales Through Dealers and Carriers, Street Vendors, Counter Sales, and Other Non-USPS Paid Distribution	0	0
	(4) Other Classes Mailed Through the USPS	0	0
c. Total Paid and/or Requested Circulation (<i>Sum of 15b. (1), (2),(3),and (4)</i>)		1116	1073
d. Free Distribution by Mail (<i>Samples, complimentary, and other free</i>)	(1) Outside-County as Stated on Form 3541	0	0
	(2) In-County as Stated on Form 3541	0	0
	(3) Other Classes Mailed Through the USPS	0	0
e. Free Distribution Outside the Mail (<i>Carriers or other means</i>)		32	32
f. Total Free Distribution (<i>Sum of 15d. and 15e.</i>)		32	32
g. Total Distribution (<i>Sum of 15c. and 15f.</i>)		1148	1105
h. Copies not Distributed		652	595
i. Total (<i>Sum of 15g. and h.</i>)		1800	1700
j. Percent Paid and/or Requested Circulation (<i>15c. divided by 15g. times 100</i>)		1116	1073
16. Publication of Statement of Ownership			
<input checked="" type="checkbox"/> Publication required. Will be printed in the		November 1999	issue of this publication.
			<input type="checkbox"/> Publication not required.
17. Signature and Title of Editor, Publisher, Business Manager, or Owner			Date
Dr. Ronald D. McPherson, Executive Editor 			August 17, 1999
I certify that all information furnished on this form is true and complete. I understand that anyone who furnishes false or misleading information on this form or who omits material or information requested on the form may be subject to criminal sanctions (including fines and imprisonment) and/or civil sanctions (including civil penalties).			

Instructions to Publishers

- Complete and file one copy of this form with your postmaster annually on or before October 1. Keep a copy of the completed form for your records.
- In cases where the stockholder or security holder is a trustee, include in items 10 and 11 the name of the person or corporation for whom the trustee is acting. Also include the names and addresses of individuals who are stockholders who own or hold 1 percent or more of the total amount of bonds, mortgages, or other securities of the publishing corporation. In item 11, if none, check the box. Use blank sheets if more space is required.
- Be sure to furnish all circulation information called for in item 15. Free circulation must be shown in items 15d, e, and f.
- Item 15h., Copies not Distributed, must include (1) newsstand copies originally stated on Form 3541, and returned to the publisher, (2) estimated returns from news agents, and (3), copies for office use, leftovers, spoiled, and all other copies not distributed.
- If the publication had Periodicals authorization as a general or requester publication, this Statement of Ownership, Management, and Circulation must be published; it must be printed in any issue in October or, if the publication is not published during October, the first issue printed after October.
- In item 16, indicate the date of the issue in which this Statement of Ownership will be published.
- Item 17 must be signed.

Failure to file or publish a statement of ownership may lead to suspension of Periodicals authorization.